Materials Advances

ROYAL SOCIETY OF CHEMISTRY

PAPER

View Article Online
View Journal | View Issue

Cite this: *Mater. Adv.*, 2025, **6**, 6008

Synergistic effects of Ag/g-C_3N_4-incorporated bi-metallic ZnTi-LDH in CO_2 photoreduction to hydrocarbons†

Jijoe Samuel Prabagar,[ab] C. Ashajyothi,[c] Arpan Kumar Tripathi,[d] Peter R. Makgwane,[e] Akhtar Rasool,[fg] Mohammed H Alqarni,[h] Ahmed I. Foudah,[h] Dong-Kwon Lim[a] and Harikaranahalli Puttaiah Shivaraju *[bi]

Coupling solar energy with photocatalytic processes offers a viable route to address environmental challenges such as pollution remediation and CO_2 reduction. The strategic construction of heterojunctions enhances charge separation efficiency, thereby improving photocatalytic performance. Herein, a bi-metallic ZnTi-LDH/Ag/g-C_3N_4 heterojunction photocatalyst was rationally engineered to facilitate the photoreduction of CO_2 into value-added hydrocarbon compounds, offering potential utility across energy, chemical, and environmental sectors. The distinctive peaks in the XRD patterns, along with the elemental interactions analyzed through XPS and surface atomic ratio calculations based on the XPS results, further established the successful formation of ZnTi-LDH-Ag/gC_3N_4. The composite exhibited an absorbance range within the spectrum window of 400–500 nm with a narrow bandgap of 2.13 eV, indicating its potential for photocatalysis in the visible light region. PL spectra suggested that the interface has the potential to suppress electron–hole recombination compared to pristine ZnTi-LDH and Ag/gC_3N_4. The photoreduction studies of CO_2 using this interface composite demonstrated the successful generation of 36.66 mmol L^{-1} of CH_3OH and 10.86 mmol L^{-1} of HCOOH. Notably, the selectivity of CH_3OH was 91.01% compared to 8.99% of HCOOH. The stability and recyclability test revealed consistent generation of CH_3OH and HCOOH over three cyclic runs without alteration in the interface structures. The engineered photocatalyst composite demonstrates strong activity for visible-light-driven CO_2 conversion into valuable hydrocarbons, underscoring solar energy as a viable route for both carbon mitigation and sustainable resource synthesis.

Received 17th June 2025,
Accepted 14th July 2025

DOI: 10.1039/d5ma00650c

rsc.li/materials-advances

1. Introduction

The emission of carbon dioxide (CO_2) significantly disrupts the equilibrium level of the carbon cycle within the natural environment, resulting in severe ecological issues, notably the greenhouse effect.[1] A report by the "Global Carbon Budget" stated that in 2023, global CO_2 emissions reached 36.8 billion tons, which is 1.1% higher than that in the preceding year. This highlights the immediate and eventual exhaustion of fossil fuels, which serve as the primary energy source for humanity, and the significant amount of CO_2 emissions associated with them. Potential CO_2 capture and transformation into hydrocarbon fuels has emerged as a significant area of interest in scientific research owing to its potential to offer a dual solution for the increasing CO_2 levels and the energy crisis.[2] Photocatalytic CO_2 reduction involves the direct transformation of CO_2 gas in an aqueous medium into value-added hydrocarbons by employing solar energy as the sole energy source.[3] This conversion process, discovered by Inoue *et al.*, has received

[a] *KU-KIST Graduate School of Converging Science and Technology, Korea University, 145 Anam-ro, Seongbuk-gu, Seoul 02841, Republic of Korea*
[b] *Department of Environmental Sciences, JSS Academy of Higher Education and Research, Mysuru 570015, India. E-mail: shivarajuenvi@gmail.com*
[c] *Department of P.G. Studies and Research in Biotechnology, Vijayanagara Sri Krishnadevarya University, Ballari 583105, Karnataka, India*
[d] *Faculty of Pharmaceutical Sciences, Shri Shankaraacharya Technical Campus, Bhilai 490001, Chhattisgarh, India*
[e] *Institute of Catalysis and Energy Solutions (ICES), College of Science Engineering and Technology, University of South, Private Bag X6, Florida 1710, South Africa*
[f] *Research Center for Chemistry, National Research and Innovation Agency, Jakarta, Indonesia*
[g] *Department of Biotechnology, Manav Rachna International Institute of Research and Studies, Faridabad -121004, Haryana, India*
[h] *Department of Pharmacognosy, College of Pharmacy, Prince Sattam Bin Abdulaziz University, Alkharj, Saudi Arabia*
[i] *Center for Water, Food and Energy (CWFE), GREENS TRUST, Harikaranahalli, Dombaranahalli Post, Tumkur District, Karnataka, India 572215*

† Electronic supplementary information (ESI) available. See DOI: https://doi.org/10.1039/d5ma00650c

considerable attention from energy and environmental researchers.[4] Despite the identification of various effective photocatalysts for CO_2 reduction, their limited selectivity towards desired products hinders their widespread implementation and practical applications.[5,6] Therefore, several techniques have been developed to produce a specifically tailored photocatalyst that can effectively respond to the visible light range.[7,8] These techniques incorporate ion doping, reformation of precious metals, and construction of heterojunctions.[9,10] Hydrotalcite-identical compounds, such as the well-recognized layered double hydroxides (LDHs), exhibit well-defined layered structures and unique functionalities. LDHs are represented by a common formula $[M^{2+}{}_{1-x}M^{3+}{}_{x}(OH)_2]$ $[A^{n-}x/n{\cdot}H_2O]$, where M^{2+} denotes divalent cations and M^{3+} denotes trivalent cations.[11] Recently, LDHs have gained importance as a substantial group of photocatalysts and are widely investigated for their potential in the degradation of aquatic pollutants through the oxidation separation of water molecules, as well as in CO_2 reduction.[12–15] Intrinsically, they are considered a capable alternative to conventional titanium dioxide (TiO_2) photocatalysts.[16] Subsequently, there has been considerable focus on the assessment and construction of innovative LDH-based photocatalysts that demonstrate visible-light reactions within this specific area of research. Current research suggests that the incorporation of Ti into LDHs *via* doping can significantly enhance their catalytic capabilities.[16,17] Studies have supported that LDHs containing zinc titanium demonstrate excellent photocatalytic activity when compared to conventional pristine TiO_2 and zinc oxide (ZnO).[13,18] For instance, Kumar *et al.* synthesized a novel cobalt aluminium-LDHs onto TiO_2 to study CO_2 reduction, which demonstrated an enhanced photoreduction reaction compared to pristine TiO_2.[19]

The widely studied graphitic carbon nitride (gC_3N_4) is a favourable photocatalyst offering a compelling alternative to traditional metal-based photocatalysts for numerous environmental applications.[20] This can be attributed to the notable properties of gC_3N_4, which include enhanced physicochemical properties, a narrow bandgap, an adaptable electronic configuration, economical, low toxicity, as well as proper energy states at the upper and lower limits of the bandgap that permit effective water splitting and CO_2 photoreduction.[21–23] Regardless of its potential, various challenges and restrictions still remain for the practical application of pure gC_3N_4. These include quick electron–hole pair recombination, restricted surface-to-volume ratio, and inefficient use of light energy.[24] Combining gC_3N_4 with other photocatalysts to create a heterojunction is a valuable method for enhancing the photocarrier separation generated during photocatalytic reactions.[25,26]

One of the most promising methods to suppress the recombination of photogenerated charge carriers is the creation of a heterojunction catalyst by merging dualistic dissimilar photocatalysts with appropriate band edge energies.[27] For instance, in our previous studies, we reported that coupling mixed metal oxides derived from LDH with gC_3N_4 displayed enhanced photoreduction efficiency of nitrogen to ammonia.[28] The advancement of effective and durable photocatalysts for CO_2 reduction is a significant challenge due to the complex reaction mechanism involved in this process. Despite considerable progress in this area, achieving high photocatalytic efficiency in the conversion of valuable CO_2 resources without using a sacrificial agent continues to pose a significant challenge in the field of research.[29] The major limitation is the slow redox chemistry involved in CO_2 reduction, which requires multiple electron transfer steps.[30]

To further enhance the photocatalytic reaction, a multilateral heterojunction system incorporating a noble metal can be utilized.[31] This system typically consists of a photocatalyst, a noble metal co-catalyst, and a second material that assists as an electron facilitator between the photocatalyst and the co-catalyst.[32] The photocatalytic materials absorb photons and then generate hole pairs; interfaced co-catalysts, such as noble metals, supply potential sites for efficient separation and transformation of charge carriers.[28] The photocatalytic material acts as an electron facilitator to aid the electron transport from the core catalyst to the co-catalyst. The incorporation of noble metals, including gold, silver, *etc.*, into the system has demonstrated that the efficiency of visible light absorption by photocatalysts and overall efficiency can be enhanced through the influence of surface plasmon resonance (SPR) induced by noble metals.[32,33] When the noble metal nanoparticles absorb photons, they produce cooperative oscillations of conduction electrons known as plasmons.[34] The plasmons can interact with the incident light and enhance the absorption of photons, spreading the absorption range of the catalyst into the visible spectral band. Moreover, the presence of noble-metallic elements can act as electron traps, enabling the charge transfer process between the photocatalysts. It apparently enhances the separation and mobility of photon-generated charge carriers while limiting the recombination rate, thereby leading to an increase in photocatalytic efficiency. Silver is a better choice in this case compared to other noble metals as it possesses an extended electronic lifetime and is also cost-effective.[35] Silver exhibits lower ohmic losses in the frequency range of visible light, which results in a better availability of light energy for plasmonic excitation and less heat loss, resulting in a better SPR response.

In this study, bimetallic zinc–titanium layered double hydroxide (ZnTi LDH) with gC_3N_4 and silver (Ag) was synthesized *via* a hydrothermal technique, light-assisted deposition and self-assembly process. Advanced characterization techniques were employed to investigate the properties and functionalities of the synthesized interfaced catalysts, which were analyzed in detail for optimized use in photocatalysis. The synthesized photocatalyst interface composite is capable of effectively utilizing visible light energy for desired photocatalytic reactions. This is evidenced by the photoreduction performance evaluation of CO_2 conducted under a light-emitting diode (LED) source, which only allows visible light. Based on our understanding, this is the initial documentation on employing the layered interface of gC_3N_4 nanosheets with Ag and ZnTi-LDH for the photochemical transformation of CO_2 into hydrocarbons driven by an LED light source (visible spectrum) as a potential energy source.

2. Methodology

2.1. Fabrication of ZnTi LDH, g-C_3N_4, Ag/gC_3N_4 and ZnTi LDH/gC_3N_4/Ag

Titanium tetrachloride ($TiCl_4$) was mixed with zinc dinitrate hexahydrate (Zn $(NO_3)_2$ $6H_2O$) using deionized water in a beaker, and then urea was introduced into the mixture with continuous agitation until it dissolved completely. Urea acts as a slow-releasing agent and increases the pH through hydrolysis, enabling controlled co-precipitation of ZnTi LDH. The obtained mixture was aged at 130 °C using a hydrothermal autoclave with Teflon liners for 48 h to allow the precipitation of the ZnTi LDH precursor. After the ageing process, the precipitate was separated *via* filtration and washed continuously under a deionized water flow. Finally, the ZnTi LDH precursor was dried at room temperature and then in a hot air oven at 60 °C. This precursor was further processed to form the desired ZnTi LDH material for various applications, and the synthesis scheme is shown in Fig. 1(a). gC_3N_4 was synthesized by calcining a specific amount of pure urea in a crucible at 500 °C for three hours (Fig. 1(b)). The resultant product obtained was a yellow powder of gC_3N_4, which was then carefully collected and cooled to room temperature, then ground into a fine powder for its planned usage.

The fabrication of Ag/gC_3N_4 powder is discussed and illustrated in Fig. 1(c). The initial step involved dissolving the gC_3N_4 powder in a solvent mixture of ethanol and water, which was then ultrasonicated for 30 min. This ensures that the gC_3N_4 particles are uniformly dissolved in the solvent. Next, a specified amount of $AgNO_3$ solution was added to the suspension, and the mixture was illuminated with an LED lamp (30 W, 128 amp, ~3000 lm) for 30 min while being constantly agitated. This process was likely a photocatalytic reaction, where the gC_3N_4 particles act as a catalyst, and the $AgNO_3$ serves as a precursor for the generation of Ag. After the reaction was accomplished, the subsequent precipitate was separated from the mixture by centrifugation and washed thoroughly. Lastly, the precipitate was dried at room temperature, followed by heating in a dust-free hot air oven at 60 °C to attain the final product.

Finally, ZnTi-LDH/gC_3N_4/Ag integration was achieved through a self-assembly technique, following a previous report with slight modification.[32] This involves the blending of two colloidal solutions independently prepared from ZnTi LDH and Ag/gC_3N_4 powder in deionized water. The blend was then stirred for 24 h to allow for a thorough self-assembly process. Self-assembly implies the process by which the distinct element of a material spontaneously assembles into a distinct structure. After the self-assembly reaction is accomplished, the subsequent solid material is separated from the mixture through centrifugation. The obtained material is then washed to remove any residual contamination and dried at 60 °C using a hot air oven to attain the final ZnTi-LDH/gC_3N_4/Ag composite.

Several characterization techniques were employed to determine the chemical, physical, and other intrinsic characteristics of the catalyst. To examine the morphology of the interfaced catalytic composite, a scanning electron microscope equipped

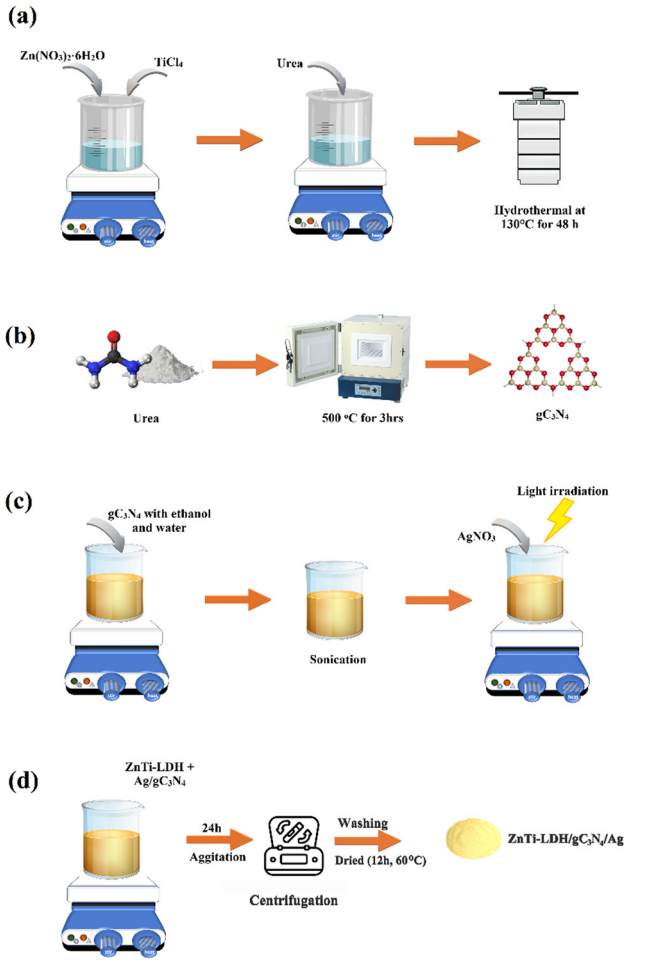

Fig. 1 Graphical representation of the synthesis of (a) ZnTi LDH precursors, (b) gC_3N_4, (c) Ag/gC_3N_4 and (d) ZnTi-LDH/gC_3N_4/Ag interface composite.

with a field emission analyzer (JEOL JSM-7100F plus) and accompanied by elemental analysis using EDX (Zeiss EVO LS 15) was used. Powder X-ray diffraction (XRD) analysis was conducted to study the crystallography of the catalyst with Cu-Kα radiation at a wavelength of 0.154 nm on a Microstar Proteum 8 (Bruker). Elemental interaction was observed using XPS with a PHI 5000 VersaProbe III system. Structural elucidation and functional arrangement were investigated using FTIR spectroscopy performed on a Bruker Alpha-200619 spectrometer with KBr and scanning in the range of 4000–400 cm^{-1}. The absorption spectra were recorded using an Agilent Cary 60 UV-vis spectrometer, whereas photoluminescence (PL) data were obtained using a Horiba Jobin Yvon FL-1039/40 spectrofluorometer. Photo-electro-chemical properties, CV-cyclic voltammetry and EIS-electrochemical impedance spectroscopy were studied using a Metrohm Autolab tool (CH Instrument, USA).

2.2. Photoreduction of CO_2

The experiment aims to convert CO_2 into hydrocarbons using a photocatalysis method. The photochemical reaction was performed in a three-mouthed photoreactor using a known

quantity of the synthesized catalyst dispersed in a 0.025 M sodium hydroxide solution in an aqueous medium. The pH of the solution was maintained at 7 during the experiment, and CO_2 was bubbled till saturation. The reaction mixture was then subjected to a light source from a 30 W LED lamp (placed ~15 cm above the reaction mixture) with a current of 128 mA and a brightness of around 3000 lumens. The reaction was controlled for 4 hours, with the reaction temperature maintained at a low level by an external cold-water flow. After the reaction was complete, the hydrocarbons produced were examined using LC-MS-MS (Agilent, US) in positive ion mode. This analytical method facilitated the identification and quantification of the produced hydrocarbon.

3. Results and discussions

3.1. Material characterization

Fig. 2(a) illustrates the XRD pattern of the synthesized catalysts. The XRD peak of Ag/gC_3N_4 displayed a peak at a 2θ angle of 27.43°, which corresponds to a particular crystal plane of (002) assigned to the material gC_3N_4 (JCPDS no. 87-1526).[36,37] However, no distinctive peaks of Ag are observed on the XRD data of Ag/gC_3N_4, which suggests the minimal filling dose and enhanced diffusion of Ag in the amalgamate.[38] The pristine ZnTi LDH spectrum is consistent with the previously reported literature. The peaks at 12.92°, 25.36°, and 38.68° can be assigned to the (003), (006), and (015) planes of the ZnTi LDH phase, respectively (JCPDS no. 20-1437).[39,40] The ZnTi LDH/gC_3N_4/Ag composite contains multiple phases. The peak at 12.83° corresponds to the (003) plane of the ZnTi LDH phase.[41] Comparing the XRD pattern of the ZnTi LDH/gC_3N_4/Ag composite to that of the pristine ZnTi LDH, it appears that the addition of gC_3N_4 and Ag has no influence on the LDH structure, which is confirmed by calculating the basal (003) spacing of the pristine LDH at 12.83°, exhibiting a *d*-spacing of 0.382 nm, whereas the composite also exhibits a similar *d*-spacing of 0.384 nm.[42]

The functional group entities of the engineered catalyst were determined from the FTIR spectra (Fig. 2(b)). FTIR spectrum of Ag/gC_3N_4 displays a broad peak around 3200 cm^{-1}, suggesting the N–H stretching.[43] The stretching vibrations of C=N are assigned to the bands observed at 1561 and 1632 cm^{-1}. The cluster of absorption bands from 1256 to 1420 cm^{-1} is due to the stretching vibrations of C–N arising from C–N (–C)–C as well as coupling C–NH–C entities found in the C_3N_4 structure.[44] Notably, Ag had no impact on the gC_3N_4 bond. The broad peak around 3248 cm^{-1} observed in the ZnTi LDH FTIR spectra signifies the presence of stretching related to the OH mode.[45] The distinctive peaks at 1397 and 1509 cm^{-1} are assigned to the intercalated carbonate entities.[46] The initial peak observed at a frequency of 1373 cm^{-1} relates to the v_3 vibration mode of the C–O double bond, explicitly involving the asymmetric stretching of the bond. The more substantial peak detected at 1501 cm^{-1} is indicative of the CO_3^{2-} anion engaging with the OH groups present in the LDH cationic sheet.[47] In the case of ZnTi LDH/gC_3N_4/Ag, the composite has similar bands to those of Ag/gC_3N_4, suggesting that the chemical structure of gC_3N_4 in the hybrid material remained intact during the self-assembly procedure.

The elemental interaction of the synthesized catalysts was explored using XPS, and the XPS data of Ag/gC_3N_4 are presented in Fig. 3. The C 1s spectrum displays two prominent peaks corresponding to specific chemical bonds in the sample (Fig. 3(a)). The peak at 285.06 eV is attributed to the sp^3 hybridized carbon atom in C–C bonds, which implies that the carbon atoms are bonded together in a tetrahedral geometry.[48] The second peak observed at 284 eV corresponds to the sp^2 hybridized nitrogen atoms within the N–C=N bonds, which suggests that the nitrogen and carbon atoms are arranged in a planar geometry with a partial double bond character.[49] The peak observed at 284.49 eV in the C 1s spectrum corresponds to

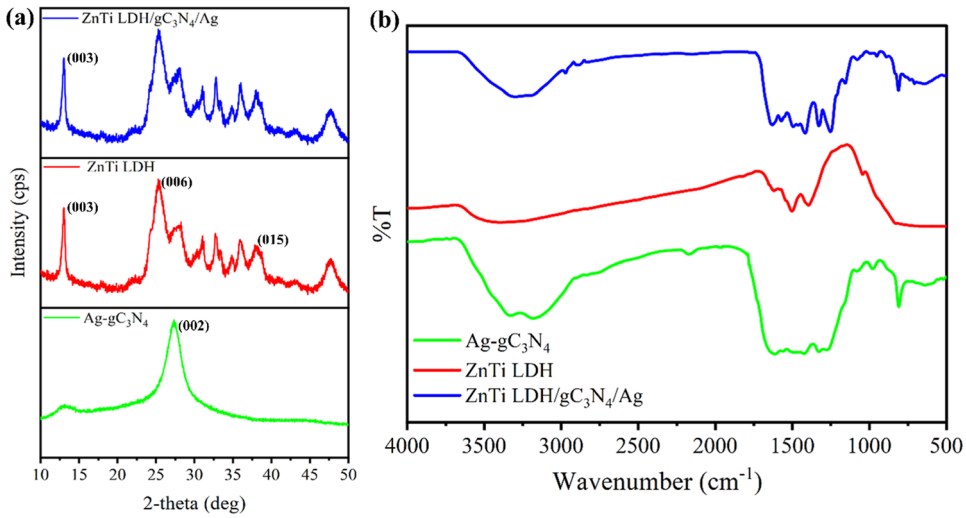

Fig. 2 (a) Powder X-ray patterns (XRD) and (b) Fourier transmission infrared spectroscopic patterns (FTIR) of ZnTi LDH, Ag/gC_3N_4, and ZnTi LDH/gC_3N_4/Ag.

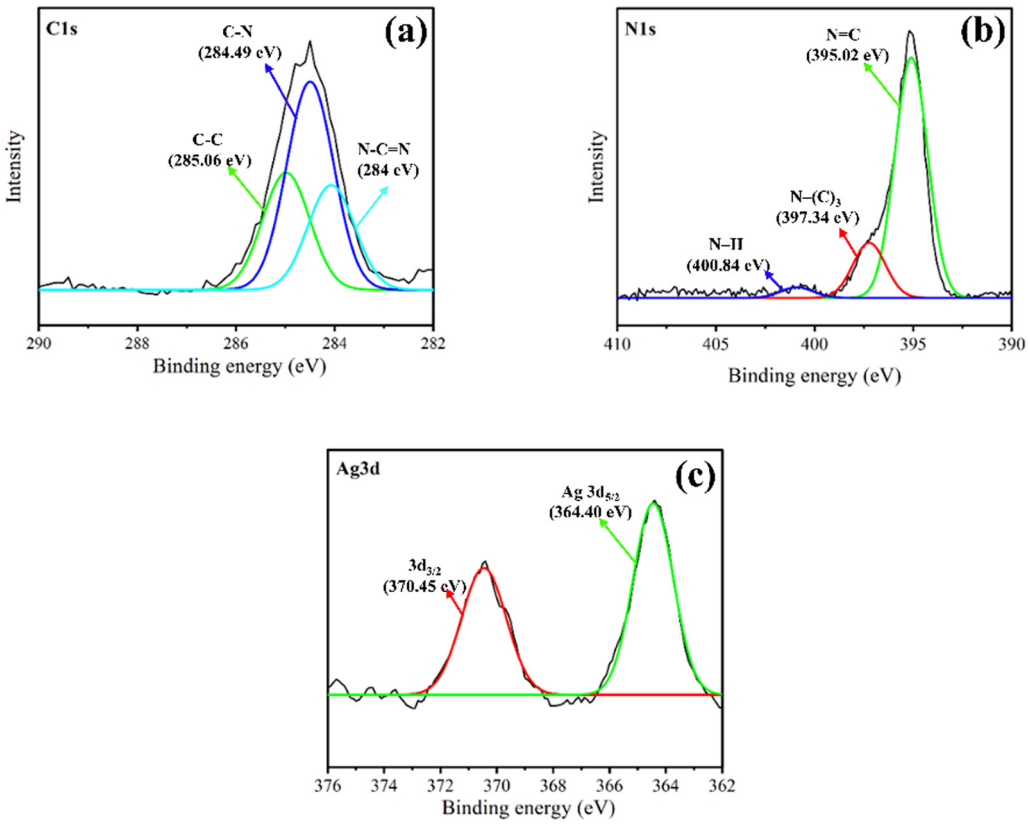

Fig. 3 X-ray photo-electroscopic spectra (XPS). (a) C 1s, (b) N 1s and (c) Ag 3d of Ag/gC_3N_4.

the sp^3 hybridized carbon–nitrogen (C–N) bond in the amine cluster of the C_3N_4 structure.[50] This peak arises from the electrons in the carbon atom bonding with the nitrogen atom in a tetrahedral arrangement, resulting in a specific energy level for the C 1s electron when excited. The N 1s band displays dual distinct peaks at 395.02 eV and 397.34 eV, which correspond to different chemical environments involving nitrogen atoms in the sample (Fig. 3(b)). The N=C bond is attributed to the peak observed at 395.02 eV, which is commonly observed in various nitrogen-containing functional groups such as nitriles, isocyanates, and imines.[50] The nitrogen atom in this type of bond is typically sp-hybridized, with a partially double-bonded character. On the other hand, the 397.34 eV peak corresponds to the N–$(C)_3$ bond, which is characteristic of tertiary amines, where the nitrogen atom is bonded to three carbon atoms.[51] This type of nitrogen atom is typically sp^3 hybridized and has a tetrahedral geometry. The peak at 400.84 eV corresponds to the N–H bonds. The Ag 3d spectrum displays two distinct peaks (Fig. 3(c)) positioned at 364.40 eV (Ag $3d_{5/2}$) and 370.45 eV (Ag $3d_{3/2}$), in agreement with the individual sublevels. This is consistent with the energy involved in binding metallic silver in its zero-oxidation state.[52] Therefore, the data confirms that the sample being analyzed is composed of metallic silver. The fact that the observed peaks in the Ag 3d spectrum match the Ag^0 binding energy values confirms the purity of the sample under investigation.

The observed bands of Zn $2p_{3/2}$ and Zn $2p_{1/2}$ at 1018.29 eV and 1041.60 eV, respectively (Fig. 4(a)), suggest that these energy levels are associated with the electronic transitions between the inner-shell levels of zinc atoms.[53] The presence of two peaks in the Ti 2p spectrum, at 454.9 eV and 460.54 eV, is consistent with the presence of Ti^{4+} in the sample (Fig. 4(b)). These peaks correspond to the Ti^{4+} $2p_{3/2}$ and $2p_{1/2}$ core levels, respectively.[54] The fact that the peaks are separated by approximately 5.6 eV is consistent with the spin–orbit splitting of the Ti 2p levels. The prominent peaks at different binding energies are observed for the N 1s XPS spectra (Fig. 4(c)). The C=N bond, attributed to 394.94 eV, characterizes the nitrogen atom bound to carbon through a triple bond. The C=N bond is often found in nitriles, which are organic compounds containing a cyano group (–C≡N). The peak at 397.04 eV corresponds to ternary N–$(C)_3$ bonds, which characterize the nitrogen atom bound to three carbon atoms in a tertiary amine group. The peak observed at 400.47 eV is consistent with amine N–H bonds, indicating the nitrogen atom bound to hydrogen in an amine group. The C 1s spectra display four distinct peaks observed at different binding energies (Fig. 4(d)). The peak at 283.9 eV is ascribed to the C–C bonds, corresponding to the carbon atoms that are directly bonded to other carbon atoms, such as in alkanes or other carbon-rich compounds. The C–NH bond is indicated by the peak at 284.34 eV, demonstrating the carbon atoms that are bonded to nitrogen in an amine functional group. The peak at 285.02 eV corresponds to the N–C–N bond, indicating the carbon atoms that are part of a nitrogen-containing heterocyclic ring, such as pyridine or imidazole.

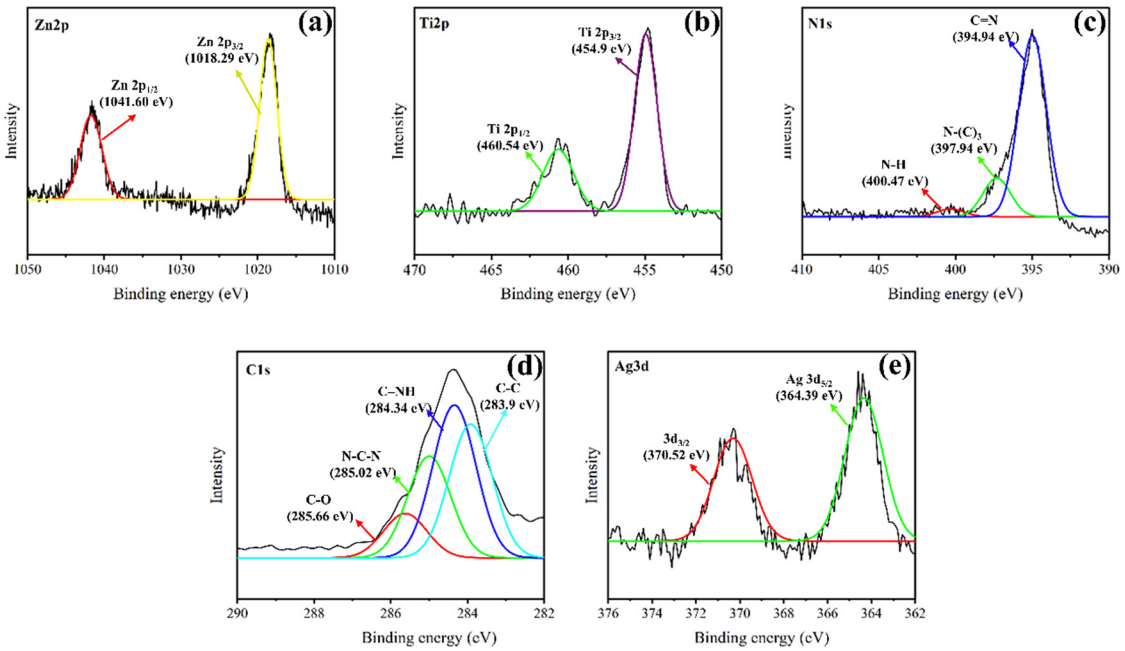

Fig. 4 XPS spectra illustrating (a) Zn 2p, (b) Ti 2p, (c) N 1s, (d) C 1s and (e) Ag 3d of ZnTi LDH/gC_3N_4/Ag.

The peak at 285.66 eV corresponds to the C–O bonds, denoting carbon atoms bonded to oxygen, such as in carbonyl or carboxyl functional groups. The Ag $3d_{5/2}$ spectrum displays a peak at 364.39 eV (Fig. 4(e)). The peak at 370.52 eV resembles to Ag $3d_{3/2}$, which corresponds to the silver atoms that are in a different chemical environment or crystal structure, leading to a slightly different binding energy compared to the first peak.

The XPS data were employed to study the surface atomic ratio. Literature states that gC_3N_4 is a covalent compound that contains nitrogen–carbon bonds and has a negative charge at a pH of 7 due to the presence of N–H and N–C functional groups, which can be ionized.[55] The negative charge on the surface of gC_3N_4 can facilitate its interaction with positively charged species, such as metal ions and can also affect its catalytic properties. On the other hand, Ag is a metal and tends to form cations (Ag^+), which are positively charged.[56] It is possible that the negative surface charge of gC_3N_4 in Ag/gC_3N_4 could repel Ag nanoparticles, causing them to aggregate or form clusters to minimize their surface area and reduce their exposure to the negatively charged gC_3N_4. This phenomenon is commonly observed in colloidal systems where particles of opposite charge can interact and form aggregates or precipitates. The negative charge on the surface of gC_3N_4 in the ZnTi LDH/gC_3N_4/Ag hybrid could be attracted to the positive charge of ZnTi LDH, as LDH materials typically have positively charged layers that can interact with negatively charged species.[32] This interaction could affect the gC_3N_4 being adsorbed on the ZnTi LDH surface, which could reveal Ag in the composite. Especially, the XPS data suggest that the Ag surface atomic ratio in the ZnTi LDH/gC_3N_4/Ag composite is ~0.525. The calculation of the Ag surface atomic ratio in the composite material indicates the existence of Ag on the surface. gC_3N_4 can undergo oxidation and generate –OH as well as –COOH groups on its surface, which can make it anionic. These functional groups can modify the surface charge and photochemical properties of gC_3N_4, including its interaction with other components in a hybrid material. For example, the negative charge on the surface of oxidized gC_3N_4 can interact with positively charged components in a hybrid material, such as metal cations or nanoparticles, through electrostatic attraction. The surface atomic ratios of C and N to the other elements on the surface of the composite were calculated to be 0.028 and 0.045, respectively, and are relative to the amount of Ti on the material surface. Based on the analysis of surface atomic concentrations, it appears that the synthesis of ZnTi LDH/gC_3N_4/Ag was effective. The surface atomic concentrations of these elements are consistent with the expected composition of the material.

Next, the morphology of ZnTi LDH/gC_3N_4/Ag was studied by employing FESEM and SEM-EDX. Fig. 5(a) and (b) illustrates the micrograph of the ZnTi LDH/gC_3N_4/Ag hybrid. The FESEM data show the incorporation of thin deposits of ZnTi LDH and gC_3N_4 micro-assembly in a ternary heterojunction with the addition of Ag. The interaction between ZnTi LDH and gC_3N_4 in the ternary heterojunction occurs through physical contact and the potential difference at the interface.[57] The integration of Ag can facilitate the activity of the heterojunction *via* enhanced electron transfer in addition to catalytic activity.[58] Briefly, the high specific surface area of ZnTi LDH permits a considerable interaction region with the gC_3N_4 microstructure, which assists in the transfer of electrons and charges between the two materials. Furthermore, the unique band structures of ZnTi LDH and gC_3N_4 can establish a potential difference at the interface of the two materials, which can initiate the relocation of electrons from one material to the other. Further, the SEM-

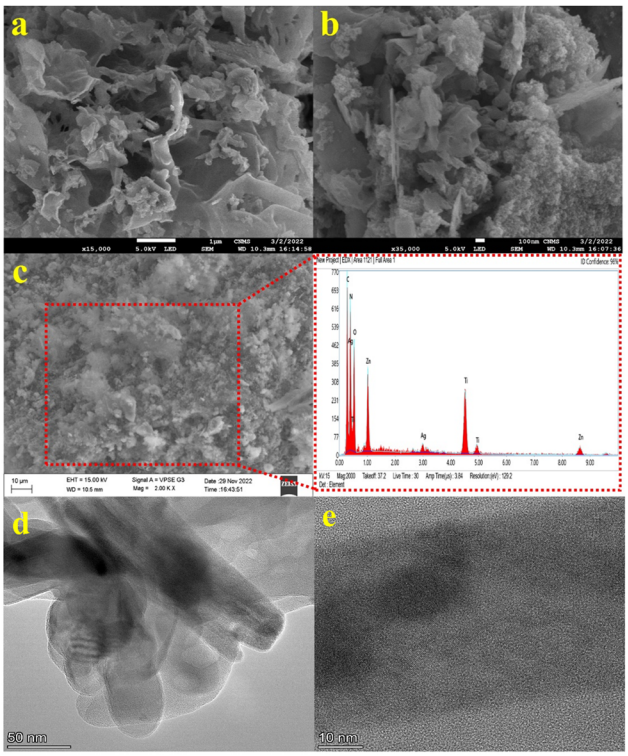

Fig. 5 (a) and (b) FESEM of ZnTi LDH/gC_3N_4/Ag revealing the formation of the heterostructure captured at ×35 000 magnification, (c) SEM-EDX of ZnTi LDH/gC_3N_4/Ag confirming the consistent distribution of all elements, (d) and (e) HR-TEM of ZnTi LDH/gC_3N_4/Ag.

EDX data is shown in Fig. 5(c), validating the existence of Zn, Ti, O, N, C and Ag. The successful assembly of the ZnTi LDH/gC_3N_4/Ag heterojunction was proven by EDX analysis, which confirmed the consistent distribution of all elements. Furthermore, HR-TEM of the synthesised ZnTi LDH/gC_3N_4/Ag is illustrated in Fig. 5(d) and (e), which confirms the formation of the composite.

The UV-Vis spectrometric data of the synthesized catalysts are displayed in Fig. 6(a). ZnTi LDH displayed UV-Vis absorbance between 200 and 350 nm. The LDH layers are responsible for strong UV absorption below ~250 nm, which may be related to the shielding effect of these layers on incident light.[59] Additionally, the incorporation of Ti into the LDH layers may contribute to absorption in the 200–350 nm range, as the 3d electrons of the Ti^{4+} ion may be involved in electronic transitions.[60] The SPR absorption around 500 nm in the Ag/gC_3N_4 and ZnTi LDH/gC_3N_4/Ag samples is consistent with the standard performance of spherical Ag nanoparticles. The surface plasmon resonance (SPR) effect is the cooperative oscillation of free electrons in Ag nanoparticles in response to incident light. This phenomenon can increase light absorption within the visible spectrum, which helps promote the generation of more electron–hole pairs and boost the effectiveness of photocatalytic processes.[61] The absorption viewed at the 400–500 nm range for the ZnTi LDH/gC_3N_4/Ag composite suggests that the integration of Ag/gC_3N_4 enhanced the light absorption of ZnTi LDH. The enhanced light absorption can be attributed to the SPR of the Ag in the interface composite, which can increase photon captivation in the visible region and lead to enhanced electron–hole generation. The presence of gC_3N_4 can also promote the expansion of photon absorption by enhancing the specific surface area and continuous charge transfer pathways. Further, the bandgaps of the catalysts were calculated utilizing Tauc plot method. As observed in Fig. 6(b), the definite bandgaps of ZnTi LDH, Ag/gC_3N_4 and ZnTi LDH/gC_3N_4/Ag are 3.55 eV, 2.39 eV and 2.13 eV, respectively. The narrowing of bandgap energy can be attributed to the heterojunction arrangement between ZnTi LDH and Ag/gC_3N_4. The localized energy levels generated by the heterojunction can influence the absorption and emission of light by the composite, resulting in changes in optical properties. Another probable reason for the apparent bandgap narrowing could be the doping effect of Ag/gC_3N_4 on ZnTi LDH. The presence of Ag/gC_3N_4 can establish new energy states within the bandgap of ZnTi LDH, which can change the absorption and emission of light by the composite.

Ag/gC_3N_4, ZnTi LDH and ZnTi LDH/gC_3N_4/Ag composite were investigated for their electrochemical properties to establish the photoinduced charge carrier separation competence. To explore the extent of charge distribution and mobility, the EIS Nyquist plots of the catalysts were initially obtained. Fig. 6(c) illustrates the impedance spectra obtained under the conditions of a 0.1 M phosphate buffer and an electrochemical mediator composed of 5 mM ferricyanide and ferrocyanide ($[Fe(CN)_6]^{3-/4-}$). The Nyquist curve for the ZnTi LDH/gC_3N_4/Ag electrode displayed a prominently reduced arc radius compared to ZnTi LDH and Ag/gC_3N_4, which implies that the composite had the lowest electron transfer resistance.[62,63] Subsequently, the composite demonstrates an increased ability for charge transfer, allowing it to effectively delay the recombination of photoinduced charges within the composite. The data from the CV, as illustrated in Fig. 6(d), signify that the ZnTi LDH/gC_3N_4/Ag composite had the highest redox current density compared to Ag/gC_3N_4 and ZnTi LDH. This indicates that in the ZnTi LDH/gC_3N_4/Ag composite, the enhanced redox current density observed in the CV supports that the composite has higher catalytic activity for CO_2 photoreduction.[64] This is attributed to various factors, such as the presence of Ag as a co-catalyst, which can increase the separation and transfer of photoinduced charge carriers, and the high surface area of the composite, which can increase the exposure of active sites to reactants.[65,66]

In addition, the synthesized interfaced composite was evaluated for its photocatalytic efficiency through photodegradation studies using methylene blue dye (5 mg L^{-1}) as a model dye. The photocatalytic reactions were first conducted in the dark to attain the adsorption–desorption equilibrium. Once the adsorption–desorption equilibrium was reached, the photocatalytic reaction mixtures were subjected to illumination from an LED light source (30 W). The aqueous dye samples were collected from the photochemical reaction vessels at two different time points (0 and 120 min) and subjected to UV-vis spectroscopic analysis for the quantitative estimation of the dye.

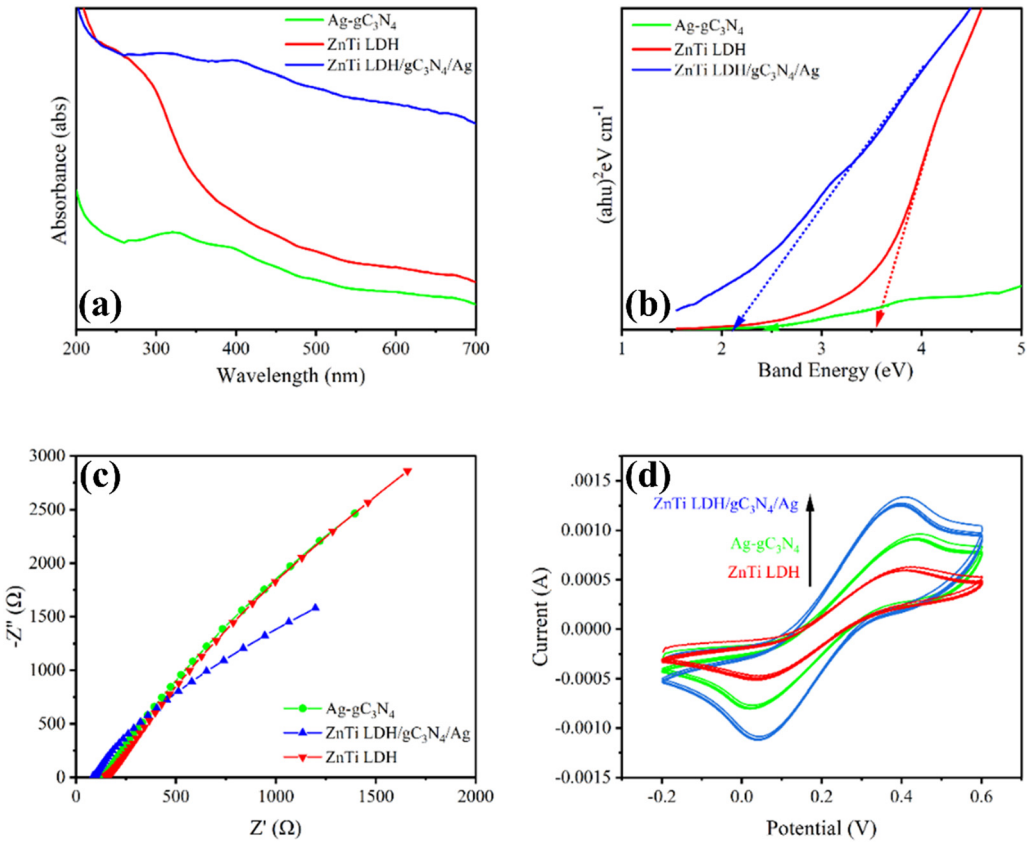

Fig. 6 (a) and (b) UV-Vis absorbance of Ag/gC_3N_4, ZnTi LDH and ZnTi LDH/gC_3N_4/Ag with direct bandgap calculation employing Tauc plot, (c) EIS and (d) CV data of Ag/gC_3N_4, ZnTi LDH and ZnTi LDH/gC_3N_4/Ag.

The spectroscopic absorbance acquired was between 550 and 750 nm, and the percentage of degradation was computed. Removal efficiencies of 50.12%, 65.75%, and 75.34% were observed for ZnTi LDH, Ag/gC_3N_4 and ZnTi LDH/gC_3N_4/Ag, respectively, suggesting that the composite is highly active under visible light illumination, similar to the pristine catalysts Fig. S1 (ESI†). After verifying the photodegradation of methylene blue, the composite was utilized for further investigation.

3.2. CO_2 photoreduction

It is evident from the above-mentioned data that ZnTi LDH/gC_3N_4/Ag exhibits enhanced photocatalytic activities under visible light sources. The photocatalytic CO_2 reduction was conducted, as referred to in Section 2.3. After the photocatalytic process had run for 4 hours, the LC-MS-MS data with positive ionization confirmed the presence of methanol (CH_3OH) and formic acid (HCOOH) at *m/z* 31.7 and 45.7, respectively, as shown in Fig. S2 (ESI†). A maximum yield of 36.66 mmol L^{-1} of CH_3OH (reaction rate, 9.16 mmol L^{-1} h^{-1}) and 10.86 mmol L^{-1} of HCOOH (reaction rate, 2.71 mmol L^{-1} h^{-1}) was achieved after the photocatalytic reaction (Fig. 7(a)). Notably, no evident peaks were observed in the controlled study (in the absence of a catalyst) (Fig. S3, ESI†).

The exploration of product selectivity offers valuable insights into the mechanisms underlying the reaction pathways. Specifically, when the number of photoinduced electrons concerned with reduction processes varies, distinct reduced products are generated. It is known that for the generation of CH_3OH and HCOOH, $6e^-$ and $2e^-$ are respectively required. The product selectivity of CH_3OH and HCOOH is 91.01% and 8.99%, respectively, with a computed electron consumption rate of 241.68 mmol L^{-1}, employing the ZnTi LDH/gC_3N_4/Ag composite. When Ag is loaded, methanol is likely to form than formic acid because it takes more electrons ($6e^-$) per product molecule than formic acid ($2e^-$).[67]

The practical utility of the catalyst was further evaluated by examining its ability to consistently generate preferred outcomes and to be recurrently utilized. The ability of ZnTi LDH/gC_3N_4/Ag to withstand visible light emitted by an LED source was investigated for 4 hours to determine its durability. The ability of the catalyst to maintain its structural and functional integrity over time was confirmed by the XRD pattern, which showed no significant alterations in the reflection peaks when compared to the initial composite run (Fig. 7(b)). Notably, the intensity of peaks in the utilized catalyst exhibits an insignificant reduction, indicating minimal changes in its structural properties. However, the composite prepared retained the integrity of the structure without any discernible alterations.[68] Subsequently, the recyclability of the catalyst was assessed under identical reaction conditions. Upon conducting three

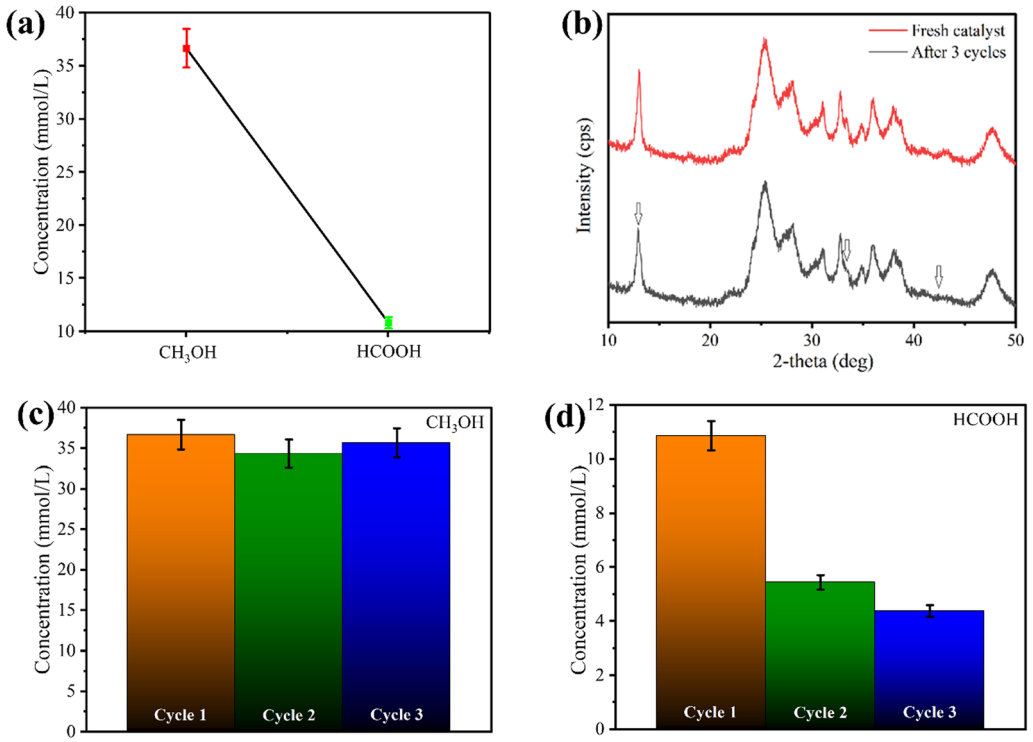

Fig. 7 (a) Generation rate of CH_3OH and HCOOH after 4 h of photocatalytic CO_2 reduction, (b) XRD pattern of fresh ZnTi LDH/gC_3N_4/Ag composite and recorded after three consecutive photoreduction cycles, and (c) and (d) recyclability study on ZnTi LDH/gC_3N_4/Ag over cyclic trials.

consecutive runs, the catalyst effectively retained CH_3OH and HCOOH, with the production rate remaining consistent (Fig. 7(c) and (d)). Interestingly, 34.33 mmol L^{-1} of CH_3OH was observed during the 2nd cycle and reduced to 35.66 mmol L^{-1} in the 3rd cycle. The HCOOH concentrations in the 2nd and 3rd cycles were 5.43 and 4.34 mmol L^{-1}, respectively, which were ~2 times and ~2.43 times less than those in the 1st cycle. The mass spectroscopic peak obtained for the recyclability study is illustrated in Fig. S4 (ESI†).

A study was conducted to explore the role of radicals in the photocatalytic reduction of CO_2 by utilizing radical scavengers. Reactive elements, such as holes and electrons, are generally neutralized by scavengers, including EDTA·2Na and $AgNO_3$. The impact of these scavengers on the CO_2 photoreduction is depicted in Fig. S5 (ESI†). The control experiment without a catalyst did not show any substantial effect on CO_2 photoreduction. A minor increase in the reaction rate was observed with the introduction of EDTA·2Na, which could be due to the generation of holes in the VB from the instant pairing of electron–hole sets. Alternatively, the reaction was hindered by the addition of $AgNO_3$, indicating the importance of the electrons in the CB in the photocatalytic transformation of CO_2 into valuable hydrocarbon derivatives.

Further, the discussion on CO_2 photoreduction using ZnTi LDH/gC_3N_4/Ag is elaborated, as illustrated in Fig. 8. The underlying photocatalytic mechanism responsible for the improved CO_2 reduction through the ZnTi LDH/gC_3N_4/Ag heterojunctions was explored and verified by PL spectra. As illustrated in Fig. 9, ZnTi LDH, Ag/gC_3N_4, and ZnTi LDH/gC_3N_4/Ag heterojunction

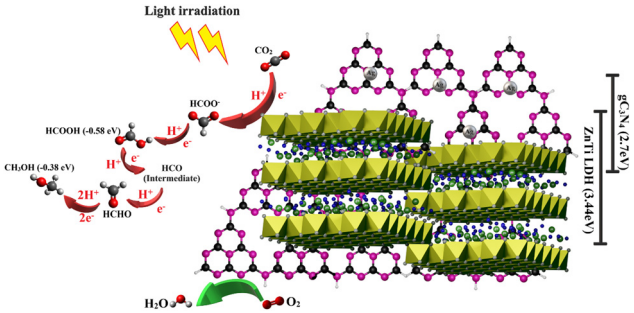

Fig. 8 Possible photocatalytic reduction mechanism of CO_2 into hydrocarbons derivatives.

exhibit a broader emission peak approximately at 440 nm. This peak is attributed to the gC_3N_4 recombination of photogenerated charge carriers and is indicative of band-band PL.[69] Here, the intensity of the PL emission is significantly greater for ZnTi LDH and Ag/gC_3N_4 compared to ZnTi LDH/gC_3N_4/Ag. The observed PL emission data suggest successful inhibition of the recombination of photogenerated electron–hole pairs in gC_3N_4, following the formation of a heterojunction with ZnTi LDH/gC_3N_4/Ag.

Additionally, the conduction band (CB) and valence band (VB) of gC_3N_4, as well as those of ZnTi-DH, were computed employing the formula:[70]

$$E_{CB} = X - 4.5 - \frac{1}{2}E_g \quad (1)$$

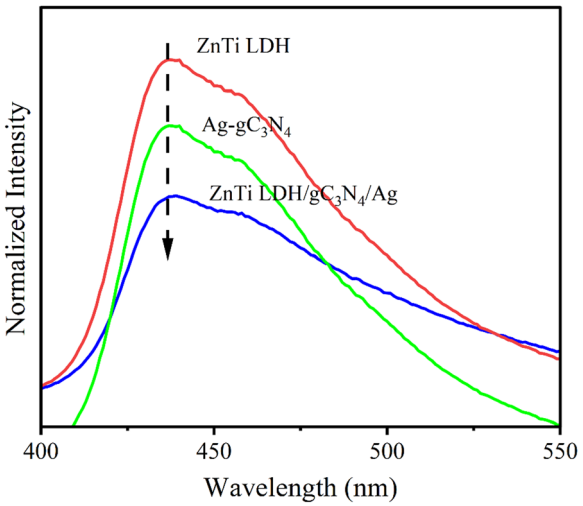

Fig. 9 PL spectra of the synthesized catalysts, where the lower peak of ZnTi LDH/gC_3N_4/Ag suggests successful inhibition of the recombination of photogenerated electron–hole pairs in the composite.

$$E_{CB} = E_{VB} - E_g \quad (2)$$

Here, the absolute electronegativity of gC_3N_4 (5.51 eV) and ZnTi LDH (5.67 eV) are represented by X, which is the electronegativity of a substance, whereas E_g represents the bandgap. By computing, the CB and VB potential edges of ZnTi LDH were obtained at −0.61 eV and 2.94 eV, respectively. Then, the CB and VB edge potentials of gC_3N_4 were computed to be −1.16 eV and 1.57 eV, respectively, while the energy gap (E_g) of gC_3N_4 was 2.70 eV.[71] The CB of ZnTi LDH has a less negative value of −0.61 eV, and the CB position of gC_3N_4 is even more negative at −1.16 eV. The bandgap energies of gC_3N_4 and ZnTi LDH fall within the visible region of the electromagnetic spectrum, resulting in the photogeneration of electrons and holes when exposed to LED light irradiation. The excited electrons in gC_3N_4 can move to the CB of ZnTi LDH at the heterojunction, and the subsequent holes in the VB of ZnTi-LDH can migrate to the VB of gC_3N_4 by intersecting the same heterojunction. This results in the mutual initiation of gC_3N_4 as well as ZnTi LDH *via* the separation of charges or curbed recombination of charges. Here, Ag, along with gC_3N_4, assists in the transfer of electrons to the CB of ZnTi LDH. The holes created in the VB of gC_3N_4, along with those transferred from the VB of ZnTi LDH, can facilitate the oxidation of water molecules that are chemically bonded to the surface of gC_3N_4, leading to the production of protons and oxygen (0.82 eV *vs.* NHE). Here, the initiation of $^{\bullet}OH$ (2.72 eV *vs.* NHE) through the photoinduced holes in the VB of ZnTi LDH also occurs. Concurrently, the photogenerated electrons on the CB of ZnTi LDH are involved in the photoreduction of CO_2 into CH_3OH and HCOOH owing to its lower potential of −0.61 eV compared to the standard reduction potentials of CH_3OH (−0.38 eV *vs.* NHE) and HCOOH (−0.58 eV *vs.* NHE). The following equation explains the above-mentioned mechanism.

$$\text{ZnTi LDH/gC}_3\text{N}_4\text{/Ag} + h\gamma \rightarrow \text{ZnTi LDH/gC}_3\text{N}_4\text{/Ag}(e^- + h^+) \quad (3)$$

$$H_2O + h^+ \rightarrow \frac{1}{2}O_2 + 2H^+ + 2e^- \quad (4)$$

$$H_2O + h^+ \rightarrow H^+ + {}^{\bullet}OH \quad (5)$$

$$CO_2 + 6H^+ + 6e^- \rightarrow CH_3OH + H_2O \quad (6)$$

$$CO_2 + 2H^+ + 2e^- \rightarrow HCOOH \quad (7)$$

The possible reduction pathway involves the initial generation of formate ion ($HCOO^-$) and HCOOH, with HCO and formaldehyde (HCHO) as intermediates that further generate ethanol.[72] Due to the two very strong double bonds that hold the carbon and oxygen atoms together, CO_2 has a very low thermodynamic inclination to react and a very low Gibbs free energy. Conversion of this stable CO_2 into CH_3OH and HCOOH required immense energy from an external source.[73] Therefore, the use of ZnTi LDH/gC_3N_4/Ag, owing to its attractive qualities, which include a narrow bandgap, inhibition of photogenerated electron–hole pairs and visible-light activity, can reduce CO_2 with improved selectivity and promising efficacy in the formation of value-added hydrocarbons.

4. Conclusion

In brief, ZnTi LDH/gC_3N_4/Ag was successfully synthesized *via* hydrothermal treatment, followed by a self-assembly approach. The XPS and FE-SEM data revealed the successful formation of the heterojunction structure. Spectrophotometric results confirmed the SPR effect, resulting from the presence of Ag nanoparticles. The photocatalytic characterization of a model dye degradation of the catalysts confirms the maximum photocatalytic activity for ZnTi LDH/gC_3N_4/Ag. Further, the ZnTi LDH/gC_3N_4/Ag exhibits notable CO_2 reduction, achieving a maximum yield of 36.66 mmol L^{-1} of CH_3OH and 10.86 mmol L^{-1} of HCOOH. The enhanced photocatalytic activity exhibited by the ZnTi LDH/gC_3N_4/Ag composite can be attributed to the interface interaction between ZnTi LDH and gC_3N_4, as well as the potent SPR influence of the Ag nanoparticles. These factors notably enhance the partition and transference competencies of photoinduced charge carriers. The heterojunctions displayed exceptional photostability, remaining highly active even after multiple experimental runs with no discernible decline in performance. In conclusion, the utilization of heterojunctions comprising LDH, gC_3N_4, and transition metal (Ag) has demonstrated efficacy in creating photocatalysts that are active under visible light. Exploring alternative materials is a promising avenue for future research. This study is anticipated to offer innovative insights and directions for designing more efficient photocatalysts.

Author contributions

Prabagar Jijoe Samuel: conceptualisation, conducting experiment, data collection and original manuscript writing. C. Ashajyothi, Arpan Kumar Tripathi, Akhtar Rasool: software and resources.

Peter R. Makgwane, Dong-Kwon Lim: validation and final manuscript proof reading. Mohammed H. Alqarni, Ahmed I. Foudah: editing and resources. Harikaranahalli Puttaiah Shivaraju: conceptualization, methodology, validation, resource and final manuscript editing.

Conflicts of interest

The authors declare that they have no conflict of interest.

Data availability

The data supporting this article have been included as part of the ESI.†

Acknowledgements

The authors extend their sincere thanks to JSS AHER and GREENS TRUST for providing laboratory facilities and other resources during this research work.

References

1 P. Jijoe Samuel, S. Yadav, T. Thinley, A. Hosakote Shankara, P. R. H. Vikram and B. M. Gurupadayya, *et al.*, Visible light irradiation driven CO_2 reduction into hydrocarbons on trimetallic based layered double hydroxide, *Mater. Today: Proc.*, 2023, **75**, 38–45, DOI: 10.1016/J.MATPR.2022.10.304.

2 S. Jiang, X. Shi, Y. Zu, F. Sun and G. Zhu, Interfacial growth of 2D MOF membranes: *Via* contra-diffusion for CO_2 separation, *Mater. Chem. Front.*, 2021, **5**, 5150–5157, DOI: 10.1039/d1qm00154j.

3 A. Ali Khan and M. Tahir, Construction of an S-Scheme Heterojunction with Oxygen-Vacancy-Rich Trimetallic CoAlLa-LDH Anchored on Titania-Sandwiched Ti_3C_2 Multilayers for Boosting Photocatalytic CO_2 Reduction under Visible Light, *Ind. Eng. Chem. Res.*, 2021, **60**, 16201–16223, DOI: 10.1021/acs.iecr.1c03242.

4 T. Inoue, A. Fujishima, S. Konishi and K. Honda, Photoelectrocatalytic reduction of carbon dioxide in aqueous suspensions of semiconductor powders, *Nature*, 1979, **277**, 637–638, DOI: 10.1038/277637a0.

5 R. deRichter and S. Caillol, Fighting global warming: The potential of photocatalysis against CO_2, CH_4, N_2O, CFCs, tropospheric O_3, BC and other major contributors to climate change, *J. Photochem. Photobiol., C*, 2011, **12**, 1–19, DOI: 10.1016/j.jphotochemrev.2011.05.002.

6 J. Fu, K. Jiang, X. Qiu, J. Yu and M. Liu, Product selectivity of photocatalytic CO_2 reduction reactions, *Mater. Today*, 2020, **32**, 222–243, DOI: 10.1016/J.MATTOD.2019.06.009.

7 P. Saha, S. Amanullah and A. Dey, Selectivity in Electrochemical CO_2 Reduction, *Acc. Chem. Res.*, 2022, **55**, 134–144, DOI: 10.1021/ACS.ACCOUNTS.1C00678/ASSET/IMAGES/MEDIUM/AR1C00678_0014.GIF.

8 J. Fu, K. Jiang, X. Qiu, J. Yu and M. Liu, Product selectivity of photocatalytic CO_2 reduction reactions, *Mater. Today*, 2020, **32**, 222–243, DOI: 10.1016/J.MATTOD.2019.06.009.

9 Y. Chen, W. Huang, D. He, Y. Situ and H. Huang, Construction of heterostructured g-C_3N_4/Ag/TiO_2 microspheres with enhanced photocatalysis performance under visible-light irradiation, *ACS Appl. Mater. Interfaces*, 2014, **6**, 14405–14414, DOI: 10.1021/AM503674E/SUPPL_FILE/AM503674E_SI_001.PDF.

10 J. S. Prabagar, K. L. Reddy and D.-K. Lim, Visible-Light Responsive Gold Nanoparticle and Nano-sized Bi_2O_{3-x} Sheet Heterozygote Structure for Efficient Photocatalytic Conversion of N_2 to NH_3, *Chin. J. Struct. Chem.*, 2025, **44**(4), 100564, DOI: 10.1016/J.CJSC.2025.100564.

11 P. S. Jijoe, S. R. Yashas and H. P. Shivaraju, Fundamentals, synthesis, characterization and environmental applications of layered double hydroxides: a review, *Environ. Chem. Lett.*, 2021, **19**, 2643–2661, DOI: 10.1007/s10311-021-01200-3.

12 J. S. Prabagar, Y. Sneha, T. Tenzin, B. Shahmoradi, S. Rtimi and K. Wantala, *et al.*, Photocatalytic transfer of aqueous nitrogen into ammonia using nickel-titanium-layered double hydroxide, *Environ. Sci. Pollut. Res.*, 2022, **2022**, 1–11, DOI: 10.1007/S11356-022-24726-7.

13 P. Gholami, A. Khataee, R. D. C. Soltani, L. Dinpazhoh and A. Bhatnagar, Photocatalytic degradation of gemifloxacin antibiotic using Zn-Co-LDH@biochar nanocomposite, *J. Hazard. Mater.*, 2020, **382**, 121070, DOI: 10.1016/j.jhazmat.2019.121070.

14 C. Zhu, Y. Wang, L. Qiu, W. Yang, Y. Yu and J. Li, *et al.*, *Z*-scheme NiFe LDH/$Bi_4O_5I_2$ heterojunction for photo-Fenton oxidation of tetracycline, *J. Alloys Compd.*, 2023, 169124, DOI: 10.1016/J.JALLCOM.2023.169124.

15 Q. Shi, X. Zhang, Y. Yang, J. Huang, X. Fu and T. Wang, *et al.*, 3D hierarchical architecture collaborating with 2D/2D interface interaction in NiAl-LDH/Ti_3C_2 nanocomposite for efficient and selective photoconversion of CO_2, *J. Energy Chem.*, 2021, **59**, 9–18, DOI: 10.1016/J.JECHEM.2020.10.038.

16 S. Zhang, Z. Liu, D. Chen, Z. Guo and M. Ruan, Oxygen vacancies engineering in TiO_2 homojunction/ZnFe-LDH for enhanced photoelectrochemical water oxidation, *Chem. Eng. J.*, 2020, **395**, 125101, DOI: 10.1016/j.cej.2020.125101.

17 D. Wang, N. Ge, S. Qian, J. Li, Y. Qiao and X. Liu, Selenium doped Ni-Ti layered double hydroxide (Ni-Ti LDH) films with selective inhibition effect to cancer cells and bacteria, *RSC Adv.*, 2015, **5**, 106848, DOI: 10.1039/c5ra18740k.

18 M. Shao, J. Han, M. Wei, D. G. Evans and X. Duan, The synthesis of hierarchical Zn-Ti layered double hydroxide for efficient visible-light photocatalysis, *Chem. Eng. J.*, 2011, **168**, 519–524, DOI: 10.1016/j.cej.2011.01.016.

19 S. Kumar, L. J. Durndell, J. C. Manayil, M. A. Isaacs, C. M. A. Parlett and S. Karthikeyan, *et al.*, Delaminated CoAl-Layered Double Hydroxide@TiO_2 Heterojunction Nanocomposites for Photocatalytic Reduction of CO_2, *Part. Part. Syst. Charact.*, 2018, **35**(1), 1700317, DOI: 10.1002/PPSC.201700317.

20 M. Aggarwal, S. Basu, N. P. Shetti, M. N. Nadagouda, E. E. Kwon and Y. K. Park, *et al.*, Photocatalytic carbon dioxide reduction: Exploring the role of ultrathin 2D graphitic

carbon nitride (g-C_3N_4), *Chem. Eng. J.*, 2021, **425**, 131402, DOI: 10.1016/J.CEJ.2021.131402.

21 M. Jiménez-Salcedo, M. Monge and M. T. Tena, The photocatalytic degradation of sodium diclofenac in different water matrices using g-C_3N_4 nanosheets: A study of the intermediate by-products and mechanism, *J. Environ. Chem. Eng.*, 2021, **9**, 105827, DOI: 10.1016/J.JECE.2021.105827.

22 Y. Zhao, H. Shi, D. Yang, J. Fan, X. Hu and E. Liu, Fabrication of a Sb_2MoO_6/g-C_3N_4 Photocatalyst for Enhanced RhB Degradation and H_2 Generation, *J. Phys. Chem. C*, 2020, **124**, 13771–13778, DOI: 10.1021/ACS.JPCC.0C03209/SUPPL_FILE/JP0C03209_SI_002.PDF.

23 B. Tahir, M. Tahir and N. Kumar, Synergistic effect of gold NPs modified graphitic carbon nitride nanotubes (g-CNT) with the role of hot electrons and hole scavengers for boosting solar hydrogen production, *Int. J. Hydrogen Energy*, 2023, **48**, 15504–15521, DOI: 10.1016/J.IJHYDENE.2022.12.330.

24 H. Wang, X. Zhang, J. Xie, J. Zhang, P. Ma and B. Pan, *et al.*, Structural distortion in graphitic-C_3N_4 realizing an efficient photoreactivity, *Nanoscale*, 2015, **7**, 5152–5156, DOI: 10.1039/C4NR07645A.

25 J. Zhang, Q. Zhu, L. Wang, M. Nasir, S. H. Cho and J. Zhang, g-C_3N_4/CoAl-LDH 2D/2D hybrid heterojunction for boosting photocatalytic hydrogen evolution, *Int. J. Hydrogen Energy*, 2020, **45**, 21331–21340, DOI: 10.1016/j.ijhydene.2020.05.171.

26 D. Sun, D. Chi, Z. Yang, Z. Xing, J. Yin and Z. Li, *et al.*, Mesoporous g-C_3N_4/Zn–Ti LDH laminated van der Waals heterojunction nanosheets as remarkable visible-light-driven photocatalysts, *Int. J. Hydrogen Energy*, 2019, **44**, 16348–16358, DOI: 10.1016/J.IJHYDENE.2019.04.275.

27 S. Tonda, S. Kumar, M. Bhardwaj, P. Yadav and S. Ogale, G-C_3N_4/NiAl-LDH 2D/2D Hybrid Heterojunction for High-Performance Photocatalytic Reduction of CO_2 into Renewable Fuels, *ACS Appl. Mater. Interfaces*, 2018, **10**, 2667–2678, DOI: 10.1021/ACSAMI.7B18835/SUPPL_FILE/AM7B18835_SI_001.PDF.

28 J. S. Prabagar, D. Vinod, Y. Sneha, K. M. Anilkumar, S. Rtimi and K. Wantala, *et al.*, Novel gC_3N_4/MgZnAl-MMO derived from LDH for solar-based photocatalytic ammonia production using atmospheric nitrogen, *Environ. Sci. Pollut. Res.*, 2022, 1–14, DOI: 10.1007/S11356-022-24997-0/METRICS.

29 L. Liu, J. Qu, T. N. Maraseni, Y. Niu, J. Zeng and L. Zhang, *et al.*, Household CO_2 emissions: Current status and future perspectives, *Int. J. Environ. Res. Public Health*, 2020, **17**, 1–19, DOI: 10.3390/ijerph17197077.

30 H. Li, C. Li, L. Han, C. Li and S. Zhang, Photocatalytic reduction of CO_2 with H_2O on CuO/TiO_2 catalysts, *Energy Sources, Part A*, 2016, **38**, 420–426, DOI: 10.1080/15567036.2011.598910.

31 Y. Zhu, R. Zhu, G. Zhu, M. Wang, Y. Chen and J. Zhu, *et al.*, Plasmonic Ag coated Zn/Ti-LDH with excellent photocatalytic activity, *Appl. Surf. Sci.*, 2018, **433**, 458–467, DOI: 10.1016/j.apsusc.2017.09.236.

32 P. R. Lestari, T. Takei and N. Kumada, Novel ZnTi/C_3N_4/Ag LDH heterojunction composite for efficient photocatalytic phenol degradation, *J. Solid State Chem.*, 2021, **294**, 121858, DOI: 10.1016/J.JSSC.2020.121858.

33 T. Thinley, S. Yadav, J. Samuel Prabagar, A. Hosakote, K. M. Anil Kumar and H. P. Shivaraju, Facile synthesis of $MnTiO_3$/Ag/gC_3N_4 nanocomposite for photocatalytic degradation of tetracycline antibiotic and synthesis of ammonia, *Mater. Today: Proc.*, 2023, **75**, 24–30, DOI: 10.1016/J.MATPR.2022.10.232.

34 M. Wang, M. Ye, J. Iocozzia, C. Lin and Z. Lin, Plasmon-Mediated Solar Energy Conversion *via* Photocatalysis in Noble Metal/Semiconductor Composites, *Adv. Sci.*, 2016, **3**, 1600024, DOI: 10.1002/advs.201600024.

35 Y. Li, Q. Liao, W. Hou and L. Qin, Silver-Based Surface Plasmon Sensors: Fabrication and Applications, *Int. J. Mol. Sci.*, 2023, **24**, 4142, DOI: 10.3390/IJMS24044142.

36 S. Liu, T. Ye, Y. Liu, H. Cheng and X. Liu, Graphitic-carbon nitride nanosheets as a new inorganic filler for improving energy storage density of PVDF-based dielectric composites, *J. Mater. Sci.: Mater. Electron.*, 2020, **31**, 13063–13069, DOI: 10.1007/S10854-020-03856-Z/METRICS.

37 S. M. Abdel Moneim, T. A. Gad-Allah, M. F. El-Shahat, A. M. Ashmawy and H. S. Ibrahim, Novel application of metal-free graphitic carbon nitride (g-C_3N_4) in photocatalytic reduction—Recovery of silver ions, *J. Environ. Chem. Eng.*, 2016, **4**, 4165–4172, DOI: 10.1016/J.JECE.2016.08.034.

38 T. Sun, H. Y. Jiang, C. C. Ma, F. Mao and B. Xue, Ag/g-C_3N_4 photocatalysts: Microwave-assisted synthesis and enhanced visible-light photocatalytic activity, *Catal. Commun.*, 2016, **79**, 45–48, DOI: 10.1016/J.CATCOM.2016.03.004.

39 A. Singha Roy, S. Kesavan Pillai and S. S. Ray, A Comparison of Nitrate Release from Zn/Al-, Mg/Al-, and Mg-Zn/Al Layered Double Hydroxides and Composite Beads: Utilization as Slow-Release Fertilizers, *ACS Omega*, 2023, **8**, 8427–8440, DOI: 10.1021/ACSOMEGA.2C07395/ASSET/IMAGES/LARGE/AO2C07395_0011.JPEG.

40 G. Wu, H. Shen, J. M. Li, J. Q. Guo, X. Yin and M. Mu, Syntheses of ZnTi-LDH sensitized by tetra (4-carboxyphenyl) porphyrin for accerlating photocatalytic reduction of carbon dioxide, *J. Solid State Chem.*, 2022, **309**, 122955, DOI: 10.1016/J.JSSC.2022.122955.

41 T. S. Rad, Z. Ansarian, R. D. C. Soltani, A. Khataee, Y. Orooji and F. Vafaei, Sonophotocatalytic activities of FeCuMg and CrCuMg LDHs: Influencing factors, antibacterial effects, and intermediate determination, *J. Hazard. Mater.*, 2020, **399**, 123062, DOI: 10.1016/J.JHAZMAT.2020.123062.

42 L. Tang, C. Feng, Y. Deng, G. Zeng, J. Wang and Y. Liu, *et al.*, Enhanced photocatalytic activity of ternary Ag/g-C_3N_4/$NaTaO_3$ photocatalysts under wide spectrum light radiation: The high potential band protection mechanism, *Appl. Catal., B*, 2018, **230**, 102–114, DOI: 10.1016/J.APCATB.2018.02.031.

43 T. Narkbuakaew and P. Sujaridworakun, Synthesis of Tri-S-Triazine Based g-C_3N_4 Photocatalyst for Cationic Rhodamine B Degradation under Visible Light, *Top. Catal.*, 2020, **63**, 1086–1096, DOI: 10.1007/S11244-020-01375-Z/METRICS.

44 F. Li, R. Zhao, B. Yang, W. Wang, Y. Liu and J. Gao, *et al.*, Facial synthesis of dandelion-like g-C_3N_4/Ag with high performance of photocatalytic hydrogen production, *Int. J. Hydrogen Energy*, 2019, **44**, 30185–30195, DOI: 10.1016/J.IJHYDENE.2019.09.217.

45 A. Elhalil, S. Qourzal, F. Z. Mahjoubi, R. Elmoubarki, M. Farnane and H. Tounsadi, *et al.*, Defluoridation of groundwater by calcined Mg/Al layered double hydroxide, *Emerging Contam.*, 2016, **2**, 42–48, DOI: 10.1016/J.EMCON.2016.03.002.

46 Y. Qin, L. Wang and X. Wang, A high performance sensor based on PANI/ZnTi-LDHs nanocomposite for trace NH_3 detection, *Org. Electron.*, 2019, **66**, 102–109, DOI: 10.1016/J.ORGEL.2018.12.018.

47 M. Mališová, M. Horňáček, J. Mikulec, P. Hudec and V. Jorík, FTIR study of hydrotalcite, *Acta Chim. Slovaca*, 2018, **11**, 147–156, DOI: 10.2478/ACS-2018-0021.

48 M. Folkenant, K. Nygren, P. Malinovskis, J. Palisaitis, P. O. Å. Persson and E. Lewin, *et al.*, Structure and properties of Cr–C/Ag films deposited by magnetron sputtering, *Surf. Coat. Technol.*, 2015, **281**, 184–192, DOI: 10.1016/J.SURFCOAT.2015.09.054.

49 V. Alman, K. Singh, T. Bhat, A. Sheikh and S. Gokhale, Sunlight Assisted improved photocatalytic degradation of rhodamine B using Pd-loaded g-C_3N_4/WO_3 nanocomposite, *Appl. Phys. A: Mater. Sci. Process.*, 2020, **126**, 1–9, DOI: 10.1007/S00339-020-03914-7/METRICS.

50 F. Qiao, J. Wang, S. Ai and L. Li, As a new peroxidase mimetics: The synthesis of selenium doped graphitic carbon nitride nanosheets and applications on colorimetric detection of H_2O_2 and xanthine, *Sens. Actuators, B*, 2015, **216**, 418–427, DOI: 10.1016/J.SNB.2015.04.074.

51 H. Xu, T. Zhang, Y. Gu, X. Yan, N. Lu and H. Liu, *et al.*, An electrochemical thrombin aptasensor based on the use of graphite-like C_3N_4 modified with silver nanoparticles, *Microchim. Acta*, 2020, **187**, 1–9, DOI: 10.1007/S00604-020-4111-4/METRICS.

52 S. Tonda and W. K. Jo, Plasmonic Ag nanoparticles decorated NiAl-layered double hydroxide/graphitic carbon nitride nanocomposites for efficient visible-light-driven photocatalytic removal of aqueous organic pollutants, *Catal. Today*, 2018, **315**, 213–222, DOI: 10.1016/J.CATTOD.2017.12.019.

53 N. T. Mai, T. T. Thuy, D. M. Mott and S. Maenosono, Chemical synthesis of blue-emitting metallic zinc nanohexagons, *CrystEngComm*, 2013, **15**, 6606–6610, DOI: 10.1039/C3CE40801A.

54 W. C. Peng, Y. C. Chen, J. L. He, S. L. Ou, R. H. Horng and D. S. Wuu, Tunability of p- and n-channel TiOx thin film transistors, *Sci. Rep.*, 2018, **8**, 1–11, DOI: 10.1038/s41598-018-27598-5.

55 S. Dong, Z. Zeng, W. Cai, Z. Zhou, C. Dou and H. Liu, *et al.*, The zeta potentials of g-C_3N_4 nanoparticles: Effect of electrolyte, ionic strength, pH, and humic acid, *J. Nanopart. Res.*, 2019, **21**, 1–12, DOI: 10.1007/S11051-019-4686-Z/METRICS.

56 E. Lim, J. Heo, K. H. Bowen and S. K. Kim, Polarization of electrostatic charge in neutral Ag–Au alloy clusters, *Chem. Phys. Lett.*, 2018, **709**, 7–10, DOI: 10.1016/J.CPLETT.2018.08.030.

57 J. Hu, C. Sun, L. X. Wu, G. Q. Zhao, H. Y. Liu and F. P. Jiao, Halogen doped g-C_3N_4/ZnAl-LDH hybrid as a *Z*-scheme photocatalyst for efficient degradation for tetracycline in seawater, *Sep. Purif. Technol.*, 2023, **309**, 123047, DOI: 10.1016/J.SEPPUR.2022.123047.

58 F. Chen, Q. Yang, Y. Wang, J. Zhao, D. Wang and X. Li, *et al.*, Novel ternary heterojunction photcocatalyst of Ag nanoparticles and g-C_3N_4 nanosheets co-modified $BiVO_4$ for wider spectrum visible-light photocatalytic degradation of refractory pollutant, *Appl. Catal., B*, 2017, **205**, 133–147, DOI: 10.1016/J.APCATB.2016.12.017.

59 Y. Li, L. Tang, X. Ma, X. Wang, W. Zhou and D. Bai, Synthesis and characterization of Zn-Ti layered double hydroxide intercalated with cinnamic acid for cosmetic application, *J. Phys. Chem. Solids*, 2017, **107**, 62–67, DOI: 10.1016/J.JPCS.2017.02.018.

60 X. R. Wang, Y. Li, L. P. Tang, W. Gan, W. Zhou and Y. F. Zhao, *et al.*, Fabrication of Zn-Ti layered double hydroxide by varying cationic ratio of Ti^{4+} and its application as UV absorbent, *Chin. Chem. Lett.*, 2017, **28**, 394–399, DOI: 10.1016/J.CCLET.2016.09.002.

61 C. Lu and H. Zhou, The Ag-based SPR effect drives effective degradation of organic pollutants by BiOCOOH/AgBr composites, *Adv. Powder Technol.*, 2022, **33**, 103428, DOI: 10.1016/J.APT.2022.103428.

62 S. R. Yashas, H. P. Shivaraju, G. McKay, B. Shahmoradi, A. Maleki and K. Yetilmezsoy, Designing bi-functional silver delafossite bridged graphene oxide interfaces: Insights into synthesis, characterization, photocatalysis and bactericidal efficiency, *Chem. Eng. J.*, 2021, **426**, 131729, DOI: 10.1016/j.cej.2021.131729.

63 H. Zhang, D. Yu, W. Wang, P. Gao, L. Zhang and S. Zhong, *et al.*, Construction of a novel BON-Br–AgBr heterojunction photocatalysts as a direct *Z*-scheme system for efficient visible photocatalytic activity, *Appl. Surf. Sci.*, 2019, **497**, 143820, DOI: 10.1016/J.APSUSC.2019.143820.

64 B. S. Surendra, M. Veerabhdraswamy, K. S. Anantharaju, H. P. Nagaswarupa and S. C. Prashantha, Green and chemical-engineered $CuFe_2O_4$: characterization, cyclic voltammetry, photocatalytic and photoluminescent investigation for multi-functional applications, *J. Nanostruct. Chem.*, 2018, **8**, 45–59, DOI: 10.1007/S40097-018-0253-X/FIGURES/15.

65 Z. Lian, Z. Li, F. Wu, Y. Zhong, Y. Liu and W. Wang, *et al.*, Photogenerated hole traps in metal-organic-framework photocatalysts for visible-light-driven hydrogen evolution, *Commun. Chem.*, 2022, **5**, 1–8, DOI: 10.1038/s42004-022-00713-4.

66 S. Yao, J. Wu, W. Li, R. Zheng, R. Li and Y. Chen, *et al.*, $LaCoO_3$ co-catalyst modified Ag_2CrO_4 for improved visible-light-driven photocatalytic degradation of tetracycline, *Sep. Purif. Technol.*, 2019, **227**, 115691, DOI: 10.1016/J.SEPPUR.2019.115691.

67 A. Lais, M. A. Gondal and F. F. Al-Adel, CO_2 photocatalytic reduction to fuels: Enhanced methanol selectivity by

loading Ag on $NaNbO_3$, *AIP Conf. Proc.*, 2018, **1976**, 20013, DOI: **10.1063/1.5042380/747802**.

68 Y. S. Ravindra, S. H. Puttaiah, S. Yadav and J. S. Prabagar, Evaluation of polymeric g-C_3N_4 contained nonhierarchical ZnV_2O_6 composite for energy-efficient LED assisted photocatalytic mineralization of organic pollutant, *J. Mater. Sci.: Mater. Electron.*, 2020, **31**, 16806–16818, DOI: **10.1007/S10854-020-04235-4**.

69 S. Zhao, S. Chen, H. Yu and X. Quan, g-C_3N_4/TiO_2 hybrid photocatalyst with wide absorption wavelength range and effective photogenerated charge separation, *Sep. Purif. Technol.*, 2012, **99**, 50–54, DOI: **10.1016/J.SEPPUR.2012.08.024**.

70 J. S. Prabagar, T. Tenzin, Y. Sneha, V. Divya, H. S. Anusha and B. Shahmoradi, *et al.*, Novel NiFeAl hybridized layered double hydroxide nanofibrous for photocatalytic degradation and CO2 reduction, *Mater. TODAY Sustain.*, 2024, **26**, 100773, DOI: **10.1016/J.MTSUST.2024.100773**.

71 G. Mamba and A. K. Mishra, Graphitic carbon nitride (g-C_3N_4) nanocomposites: A new and exciting generation of visible light driven photocatalysts for environmental pollution remediation, *Appl. Catal., B*, 2016, **198**, 347–377, DOI: **10.1016/J.APCATB.2016.05.052**.

72 *Conversion of Carbon Dioxide into Hydrocarbons Vol. 1 Catalysis*, ed. Asiri A. M. Inamuddin and E. Lichtfouse, 2020, p. 40, DOI: **10.1007/978-3-030-28622-4**.

73 D. T. Whipple and P. J. A. Kenis, Prospects of CO_2 utilization *via* direct heterogeneous electrochemical reduction, *J. Phys. Chem. Lett.*, 2010, **1**, 3451–3458, DOI: **10.1021/JZ1012627/ASSET/IMAGES/MEDIUM/JZ-2010-012627_0004.GIF**.